Electron-Beam Shaping in the Transmission Electron Microscope: Control of Electron-Beam Propagation Along Atomic Columns

E. Rotunno,[1] A.H. Tavabi,[2] E. Yucelen,[3] S. Frabboni,[1,4] R.E. Dunin Borkowski,[2] E. Karimi,[5] B.J. McMorran,[6] and V. Grillo[1,*]

[1]*CNR-NANO, via G Campi 213/a, I-41125 Modena, Italy*
[2]*Ernst Ruska-Centre for Microscopy and Spectroscopy with Electrons, Forschungszentrum Jülich, 52425 Jülich, Germany*
[3]*FEI Company, Europe NanoPort, Achtseweg Noord 5, 5651 GG Eindhoven, The Netherlands*
[4]*Dipartimento di Fisica Informatica e Matematica, Università di Modena e Reggio Emilia, via G Campi 213/a, I-41125 Modena, Italy*
[5]*Department of Physics, University of Ottawa, 150 Louis Pasteur, Ottawa, Ontario K1N 6N5, Canada*
[6]*Department of Physics, University of Oregon, Eugene, Oregon, USA*

(Received 17 September 2018; revised manuscript received 22 February 2019; published 22 April 2019)

We present a detailed analysis of the propagation of high-energy electron beams that have different shapes in a crystal of [100]-oriented zincblende GaN. Our study primarily focuses on Bessel beams and makes use of reformulated Bloch wave and multislice simulations. As a result of the simplicity of the momentum spectrum of a Bessel beam and the symmetry of the crystal, its propagation in the material can be described in a free-space representation, providing a deeper understanding of channeling phenomena and of probe intensity oscillation in the propagation direction. We also consider aperture-limited and Gaussian beams. The latter probes are shown to be optimal for coupling to 1*s* Bloch states and achieving minimal spreading along atomic columns.

DOI: 10.1103/PhysRevApplied.11.044072

I. INTRODUCTION

Most electron beams that are currently used in TEM are formed using a hard aperture whose radius is chosen to limit the effects of condenser lens aberrations [1,2]. The shape of the electron probe is then approximately an Airy disc, with ripples that are only visible when the spatial coherence is high (or for "unconventional" defocus values or aperture sizes) [3]. The introduction of electron vortex beams and holographic electron beam shaping [4,5] now allows electron probes with others wavefronts to be engineered. Vortex beams are characterized by staircase wavefronts and phase singularities with zeros of intensity at their centers. In spite of their exotic shapes, the radial profiles of vortex probes, which can be used for the acquisition of atomic-resolution images [6], are determined by simple hard cut offs. Recently, the use of more complicated nanofabrication schemes has allowed holographic masks to be used to manipulate the amplitudes and phases of electron probes [7–11], extending the range of beam shapes that can be engineered. For example, a Bessel beam can be formed by using a narrow ring in the aperture plane in a similar manner to the use of hollow cone illumination [12–16], while a holographic mask is currently the best approach for producing either a narrow radial momentum distribution or a nonvanishing topological charge [8]. Bessel beams are promising for high-resolution imaging and tomography, as well as for creating vortex beams with desired shapes. They allow the radial function of the electron probe to be manipulated, thereby affecting image resolution. In particular, they have narrower central peaks than conventional beams for the same maximum convergence semiangle [17]. They are also propagation invariant in vacuum and are "self-healing," meaning that they are insensitive to partial obstruction by opaque objects. The natural question arises as to whether they are insensitive to propagation inside a crystal that can be considered as a phase and amplitude object. In this context, it is relevant that Bessel beam propagation in vacuum and channeling in a material can both be represented by solutions of the paraxial Schrödinger equation, with separation of variables between in-plane and out-of-plane components.

Here, we study the propagation of Bessel and other electron beams by reformulating Bloch wave simulations based on the concept of transverse energy as the only quantum number. This approach has the advantage that it is related less strongly to probe decomposition into plane waves, allowing the new eigenstates to directly match the overall probe shape. Bloch wave analysis has previously been carried out for aperture-limited vortex beams [18,19].

*vincenzo.grillo@unimore.it

In contrast, a Bessel beam is characterized by a single value (or a narrow distribution) of the modulus of the transverse momentum. In high-symmetry conditions (e.g., with the probe exactly on an atomic column in a material that has a large separation between columns of light atoms), the influence of the azimuthal coordinate is small, simplifying the treatment of Bloch wave propagation. We choose zincblende GaN viewed along the [100] zone axis as a model material as a result of its simple symmetry, even though this allotrope of GaN is not favored thermodynamically. In this orientation, the weak potentials of the N atomic columns can be neglected when compared to those of the well-separated Ga columns. To a good approximation, the Ga columns produce an azimuthally symmetrical potential. We develop formalism for this simplified situation and consider the didactic case of the 0th-order Bessel beam in order to understand the "pendellösung" oscillation, including a damping effect that is not associated with inelastic scattering. A coupling of this effect with the discrete momentum spectrum of the Bessel beam is shown to result in a strong selection of excited Bloch states, providing the possibility to engineer the pendellösung oscillation of the probe in a STEM experiment. Shaping of the beam into an approximate $1s$ state is found to result in the minimization of diffraction-pendellösung effects in both aperture-limited and Bessel probes. We highlight the wide variety of behaviors with sample thickness that can be tailored by beam shaping.

II. GENERAL ASPECTS OF BEAM PROPAGATION

Although a full description of electron-beam propagation inside a material is complex, we base our discussion here on a simplified approach. In general, an electron beam that enters a sample can be described using a sum over different Bloch waves $b^n_{\bar{k}}(\bar{r},z) = b^n_{\bar{k}}(\bar{r})\exp(iK_z^{(n,\bar{k})}z)$, which are associated with quantum numbers n and $\bar{k}$, where n is the band and $\bar{k}$ is the two-dimensional pseudo-momentum confined to the first Brillouin zone, similar to the solid state description of conduction electrons [20].

In the case of a convergent probe in scanning TEM (STEM), each partial plane wave in the illumination cone gives rise to its own set of Bloch waves. The overall wave function can be expressed in the form [21]

$$\Psi(\bar{r},z) = \int \sum_n \varepsilon^{n,\bar{k}} A(\bar{K}_\perp) b^n_{\bar{k}}(\bar{r})\exp(iK_z^{(n,\bar{k})}z)d\bar{K}_\perp, \quad (1)$$

where $\bar{K}_\perp$ is the transverse component of the momentum of the incident electron beam, $A(\bar{K}_\perp)$ describes the aperture cut off (including any complex amplitude modulation introduced by a probe-forming hologram) and the effect of lens aberrations, and $\varepsilon^{n,\bar{k}}$ is the complex excitation for each Bloch state $b^n_{\bar{k}}(\bar{r},z)$.

For many practical purposes, an electron beam that is located on an atomic column can be described simply in terms of its two most important components:

(1) $B^{\mathrm{TB}}_{\bar{k}}(\bar{r},z)$: Single-column localized states that can be treated as being independent of the presence of other columns. This description is equivalent to the "tight binding approximation" in solids. The most fundamental examples are $1s$ ground states, which are referred to here as $B^{1s}_{\bar{k}}(\bar{r},z)$.

(2) $B^{\mathrm{HE}}_{\bar{k}}(\bar{r},z)$: Asymptotically free states, whose propagation is approximately independent of the presence of the lattice potential.

These components can be described mathematically using a superposition of Bloch states. For the bound states, the "tight binding" approximation permits the description of each state with $n=1$ and different values of $\bar{k}$ in the form $b^{1s}_{\bar{k}}(r,z) \approx b^{1s}(r)\exp(i\bar{k}\bar{r})\exp(iK_z^{1s}z)$.

The values of $K_z^{(n)}$, that is, the velocities of phase evolution along z, can be calculated by diagonalizing the Schrödinger equation in the Bloch basis. Depending on the chosen formalism, $K_z^{(n)}$ can also be related to the transverse energy using the expression

$$E_T = \frac{\hbar^2}{2m}(K^2 - K_z^{(n)2}), \quad (2)$$

where K is the total momentum. For simplicity, the transverse energy is expressed below in the form $(K_z^{(n)2} - K_z^2)$, following the approach used by Metherell [22], with the constants in Eq. (2) equal to unity. The bound states then all have positive transverse energy, while unbound states have negative values. $K_z^{(n)}$ can also be related to the "anpassung" parameter, which is the eigenvalue of the simplified Bloch diagonalization problem

$$\gamma^{(n)} = \frac{\eta}{\lambda} - K_z^{(n)}. \quad (3)$$

In Eqs. (2) and (3), E is the beam energy after subtraction of the mean inner potential contribution, λ is the electron wavelength in vacuum, η is the correction to the electron wavelength due to the mean inner potential, and m is the relativistic electron mass. Based on these relationships, we refer equivalently to $K_z^{(n)}$, anpassung, or transverse energy. The tightly bound wave function component for the $1s$ state then takes the form

$$\begin{aligned} B^{1s}_{\bar{k}}(\bar{r},z) &= \int \varepsilon^{(1s,\bar{k})} A(\bar{K}_\perp) b^{1s}_{\bar{k}}(\bar{r},z)\exp(iK_z^{(i,\bar{k})}z)d\bar{K}_\perp \\ &\approx \exp(iK_z^{1s}z)\int \varepsilon^{1s,\bar{k}} A(\bar{K}_\perp) b^{1s}(\bar{r})\exp(i\bar{k}\bar{r})d\bar{K}_\perp. \end{aligned} \quad (4)$$

The in-plane description of the Bloch state in the form $b^{1s}(\bar{r})\exp(i\bar{k}\cdot\bar{r})$ implies that there is a single (typically

Gaussian-shaped) mode $b^{1s}(\bar{r})$ that is independent of $\bar{k}$, whereas the $\bar{k}$ dependence of the full Bloch wave $b^{1s}_{\bar{k}}(r,z)$ is confined to the phase factor $\exp(i\bar{k}r)$. This approximation is similar to the $k\cdot p$ model in the solid-state theory of Bloch electrons [23].

For nearly isolated Ga columns with only a small azimuthal dependence of the excitation factors $\varepsilon^{1s,\bar{k}}$

$$B^{\mathrm{HE}}_{\bar{k}}(\bar{r},z)=\int \varepsilon^{\mathrm{HE},\bar{k}}A(\bar{K}_{\perp})\exp(iK_z^{\mathrm{HE}}\bar{r})d\bar{K}_{\perp} \tag{5}$$

and

$$K_z^{\mathrm{HE}}=\sqrt{\frac{\eta^2}{\lambda^2}-K_{\perp}^2}\approx\frac{\eta}{\lambda}\left(1-\frac{1}{2}\frac{\lambda^2}{\eta^2}K_{\perp}^2\right). \tag{6}$$

This is the so-called s state model [24,25], which is used successfully to describe dynamical scattering of electrons in a thin specimen and many channeling-related phenomena on the assumption that the crystalline potential can be neglected compared to the transverse energies of the states. This simplified approach can be used to qualitatively describe different kinds of beam propagation that result from beating between the two components.

In order to obtain a more accurate, quantitative description of beam propagation, a complete Bloch wave treatment is needed. However, Bloch wave calculations return hundreds of thousands of coefficients, which cannot be interpreted readily but must be summed together to obtain a point-to-point representation of the wave function.

Here, we propose a simpler approach for studying beam propagation in detail, and analyze the traverse energy spectrum of the excited states. Instead of using the Bloch state quantum numbers n, k where n is the only discrete variable, we label the states based on their transverse energy. States with different values of n and k are grouped together depending on their transverse energy $\tilde{E}$ to form new states [26,27].

$$B^{\tilde{E}}(\bar{r},z)=\exp(iK_z^{\tilde{E}}z)\int\sum_n \varepsilon^{n,\bar{k}}A(\bar{K}_{\perp})b^n_{\bar{k}}(\bar{r},z)\times\delta(E^{n,\bar{k}},\tilde{E})d\bar{K}_{\perp}. \tag{7}$$

Propagation inside a crystal at point $\bar{r}$ can be regarded as a consequence of the z dependent interference of states $B^{\tilde{E}}(\bar{r},z)$ with intensity $|B^{\tilde{E}}(\bar{r},z)|^2$. For many purposes, we then consider the unit-cell-averaged intensity $I(\tilde{E})=\int|B^{\tilde{E}}(\bar{r},z)|^2d\bar{r}$.

Bloch wave calculations and their spectral description are performed using our custom software B_WISE [26]. Since Bloch wave algorithms only return parameters and excitations for plane waves, our software samples a number of points in the probe and sums the results, taking into account the appropriate phase. For simplicity, we consider a perfectly aberration-corrected microscope, in which all residual aberrations are zero. The software can also produce images that represent wave functions of these energy defined states.

Examination of the intensity spectrum as a function of a state's energy provides a straightforward approach to understand the propagation of a beam. Bound states appear in the spectrum as sharp peaks, while HE states form bands whose average value provides the mean velocity of the group, as explained below. It is also possible to explain pendellösung oscillations by evaluating the dephasing of different Bloch waves. Considering a simple distribution $P(\Delta k)$ of continuum states, the amplitude of the wave function at a point (x,y) can be expressed in the form

$$\Psi(z)=\frac{1}{N}\int_{-\infty}^{+\infty}[P(\Delta k)e^{i\Delta kz}e^{ikz}-e^{ik_0z}]d\Delta k. \tag{8}$$

The actual wave function is

$$\Psi(z)=\check{P}(z)e^{ikz}+e^{ik_0z}, \tag{9}$$

where $\check{P}(z)$ is the Fourier transform of the distribution $P(\Delta k)$. The intensity then takes the form

$$I(z)=\left|\check{P}(z)\right|^2+1+2\check{P}(z)\sin((k-k_0)z), \tag{10}$$

where $\check{P}(z)$ describes damping of the pendellösung oscillation with depth. The damping of the oscillation is not due to inelastic effects. If the momenta along z are distributed, for example, according to a Gaussian profile of width δk, then the oscillation is damped over a distance $\delta z=2\pi/\delta k$.

III. RESULTS

A. Conventional aperture-limited probe

The description of a conventional (aperture-limited) probe is straightforward. Since HE states are nearly free, they behave as a probe would do in vacuum. $B^{\mathrm{HE}}_K(\bar{r},z)$states form a concentrated waist in the sample at a depth corresponding to the in-focus condition and then broaden, for geometric reasons, to a radius $R=z\alpha$, where α is the convergence semiangle. Alternatively, the component HE states can be regarded as getting out-of-phase before and after the focus condition.

Since the $B^{1s}_K(\bar{r},z)$ overall phase $\exp(iK_zz)$ evolves with z faster than that of all of the $B^{\mathrm{HE}}_K(\bar{r},z)$ states, the two states give rise to characteristic beating with frequency

$$K_z^{1s}-K_{0z}^{\mathrm{HE}}, \tag{11}$$

where K_{0z}^{HE} is the average propagation velocity over all HE states. However, since the $B^{\mathrm{HE}}_K(r,z)$ states get out

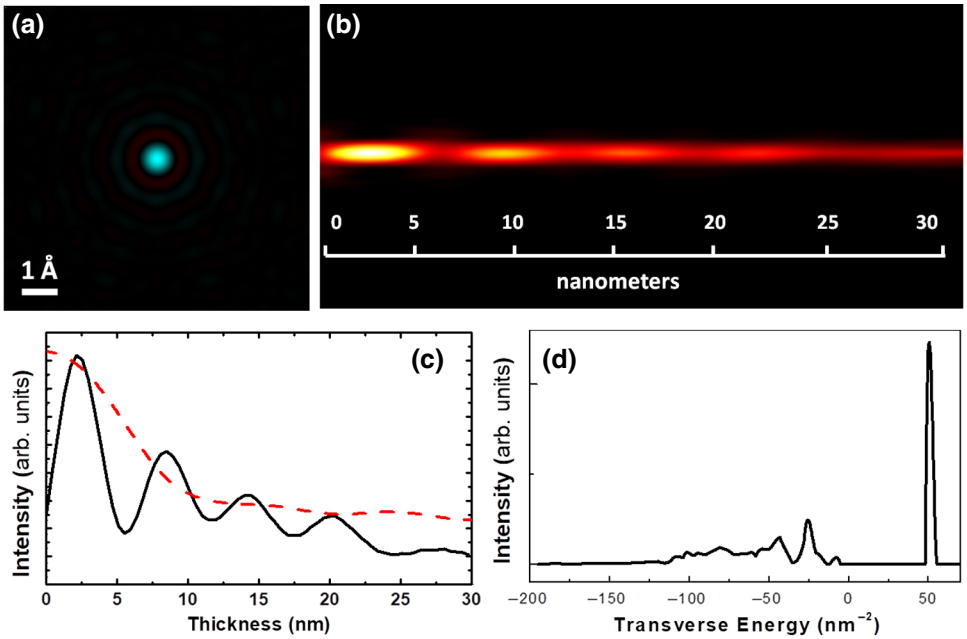

FIG. 1. (a) Calculated image of an electron probe formed by a 21-mrad aperture at 300 keV. (b) Multislice simulation of its evolution along a Ga column in a [100]-oriented GaN crystal. (c) Intensity line profile of (b) plotted as a function of depth (solid black line), shown alongside a damping profile (red dashed line) estimated according Eq. (8). (d) Transverse energy spectrum of the excited Bloch state intensities.

of phase with each other, the oscillation is damped. This point is worth emphasizing, since it is commonly believed [28,29] that damping of oscillations is due to absorption of 1*s* states, which is not considered here in Bloch wave calculations (for multislice calculation below instead we accounted for it through the "frozen lattice" approximation).

Figure 1 shows the result of a multislice simulation performed using a routine in the STEMCELL software suite [30] derived from the Kirkland multislice code [31]. The results are obtained for a [100]-oriented zincblende GaN column for a probe formed by a 21-mrad aperture at 300 keV [Fig. 1(a)] located on a Ga column. The probe intensity along the column is shown in Fig. 1(b). A characteristic channeling oscillation is visible when the intensity is plotted as a function of depth in Fig. 1(c). The traverse energy spectrum of the excited Bloch state intensities, which is calculated by sampling the probe over 1793 reciprocal points, is shown in Fig. 1(d). It is dominated by a broad band that extends roughly from -10 to -130 nm^{-2}, corresponding to eigenvalues of the $B_K^{\mathrm{HE}}(\bar{r},z)$ states. In the positive transverse energy part of the spectrum, a sharp peak at approximately 52 nm^{-2} is ascribed to the tightly bound, nondispersive 1*s* state. The 1*s* state intensity is

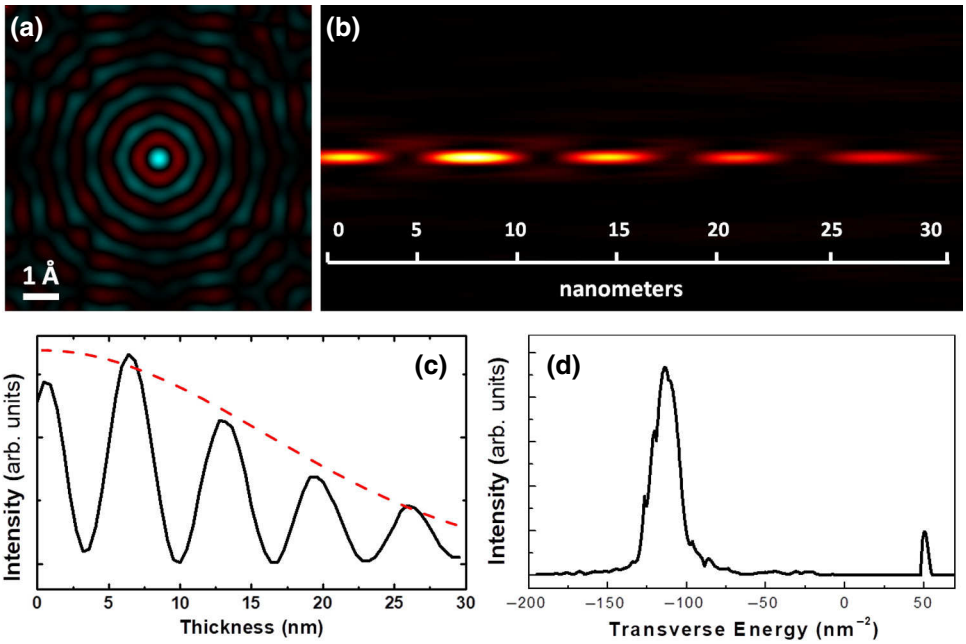

FIG. 2. (a) Calculated image of a Bessel probe formed by a 20–22-mrad ring aperture at 300 keV. (b) Multislice simulation of its evolution along a Ga column in a [100]-oriented GaN crystal. (c) Intensity line profile of (b) plotted as a function of depth (solid black line), shown alongside a damping function (red dashed curve) calculated according to Eq. (8). (d) Transverse energy spectrum of the excited Bloch state intensities.

approximately one order of magnitude higher than that of any other Bloch state, as expected for strong channeling in a crystalline solid oriented along a major zone axis. Characteristic channeling oscillations arise as a consequence of interference between the 1s Bloch states with each of the $B_K^{\mathrm{HE}}(\bar{r},z)$ states. The average transverse energy of the $B_K^{\mathrm{HE}}(\bar{r},z)$ states is approximately -80 nm^{-2}, which can be translated directly into a group velocity using Eqs. (3) and (6). Equation (11) gives the frequency of the beating. The periodicity is estimated to be approximately 8 nm, in good agreement with the multislice calculation (7.2 nm). The discrepancy (approximately 10%) results from damping due to thermal vibrations. Thermal vibrations of atoms in the lattice are responsible for absorption of the 1s state (dechanneling), which further attenuates the beating periodicity of the probe. Thermal motion is naturally included in multislice calculations, but can only be accounted for in Bloch wave calculations by using perturbative treatments or by introducing an absorptive part in the potential. We intentionally neglect any absorptive potential in our Bloch wave calculations in order to evaluate the damping produced by the simple dephasing of high-energy, unbound Bloch states.

As a result of the large spread in propagation velocity, the $B_K^{\mathrm{HE}}(\bar{r},z)$ wave packet disperses rapidly, and a damping of the oscillation can be expected, as described by Eq. (10). For a probe with larger convergence, the band is broader and greater damping results, as expected from the fact that the $B_K^{\mathrm{HE}}(\bar{r},z)$ states spread out at a faster rate. The calculated damping profile is shown as a red dashed line in Fig. 1(c) and is in good agreement with the result of the multislice calculation.

B. Bessel probe

The general form of a time-independent Bessel beam solution of order n is simply

$$\Psi(\rho,\phi,z;t) = J_n(k_\rho,\rho)e^{in\phi}e^{i(k_z\cdot z)}, \tag{12}$$

where J_n is an nth-order Bessel function of the first kind, n is an integer, the wave function's transverse and longitudinal wave vector components k_ρ and k_z, respectively, are related to its de Broglie wavelength λ by the relation $k^2 = k_\rho^2 + k_z^2 = 2m\omega/\hbar = (2\pi/\lambda)^2$, k is the modulus of the electron wavevector, and $\hbar$ is the reduced Planck constant. Here, we consider only the case $n = 0$.

Bessel probes (like plane waves) have non-normalizable intensities and can only be approximated by truncated Bessel beams that correspond to finite annulus sizes for hollow cone illumination. Here, the truncation is chosen so that most of the wave function intensity is within a single unit cell [Fig. 2(a)]. In this approximation, a Bessel

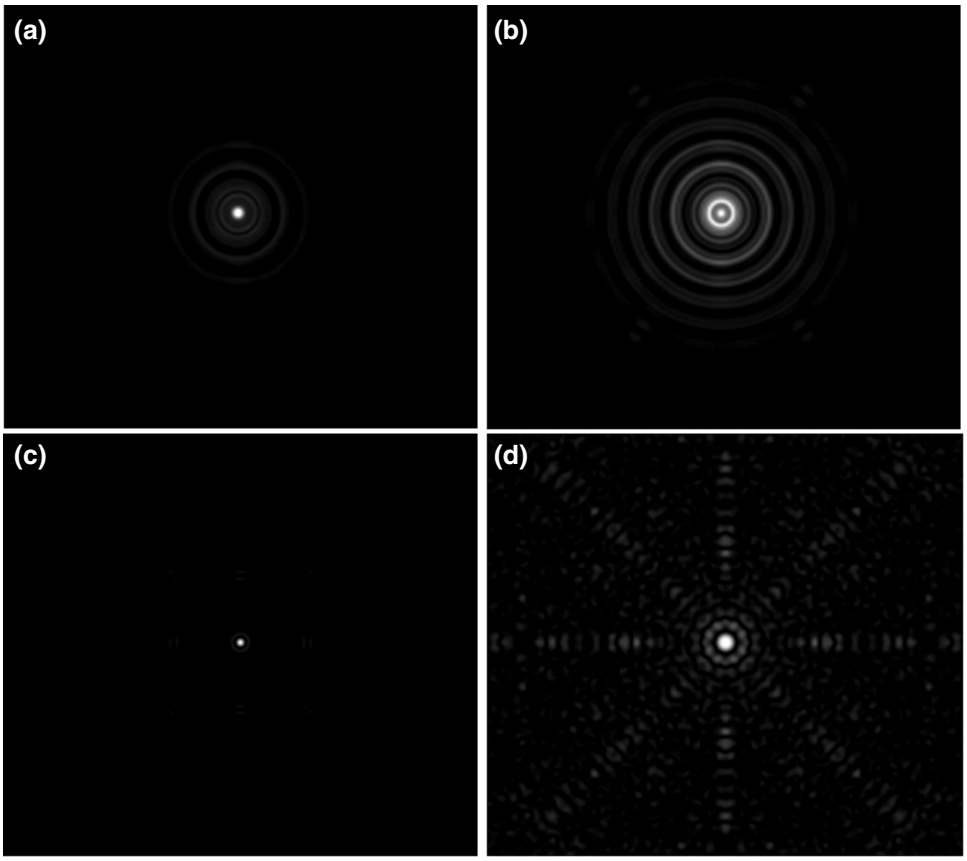

FIG. 3. Multislice simulation of a Bessel probe formed by a 20–22-mrad ring during its evolution in the specimen at depths of (a) 6 and (b) 12 nm. Bloch wave calculations of the wavefuntions corresponding to (c) the 1s state and (d) a high-energy unbound state with a transverse energy of -110 nm^{-2}.

probe propagating in vacuum has a long range of defocus for which it remains localized [32]. Similar to the vacuum case, we can assume that the $B_K^{\mathrm{HE}}(\vec{r},z)$ component of the beam does not spread along Z, as discussed in detail below.

Multislice calculations of Bessel beam propagation, which are shown in Figs. 2(b) and 2(c), display a much clearer oscillation compared to a conventional probe (Fig. 1), with nearly no damping of the oscillation in the first 30 nm of propagation. The oscillation frequency is similar, with small differences resulting from a change in the barycenter of the HE state distribution in the two cases. The intensity spectrum shown in Fig. 2(d), which is calculated by sampling the probe over 508 reciprocal points, contains a relatively narrow peak in the negative transverse energy régime at approximately -115 nm^{-2}. For an isolated column, the spectrum should be perfectly monochromatic. However, a small break in azimuthal symmetry due to the presence of N atomic columns leads to a spread in transverse energy. Nevertheless, the approximate azimuthal symmetry allows for a clear interpretation of the spectrum, which would not work for more complicated symmetries or for a small misplacement of the probe. The damping profile, which is calculated using Eq. (10), is shown in Fig. 2(c) as a red dashed line. The simple shape of the HE state band, which can be approximated as a Gaussian distribution, ensures nearly perfect quantitative agreement with the multislice calculation.

Both of these arguments can explain the results of the multislice calculations. In general, the behavior of a Bessel probe along an atomic column in a crystal is similar to propagation in vacuum, with the addition of beating with highly localized 1s states. The persistence of the oscillation is a consequence of the nondiffractive nature of a Bessel beam in vacuum and, by extension, of unbound states in crystals.

When considering the real space shapes of the $B_K^{\mathrm{HE}}(\vec{r},z)$ and $B_K^{1s}(\vec{r},z)$ components, an interesting detail becomes apparent: $B_K^{\mathrm{HE}}(\vec{r},z)$ is a Bessel function of the form

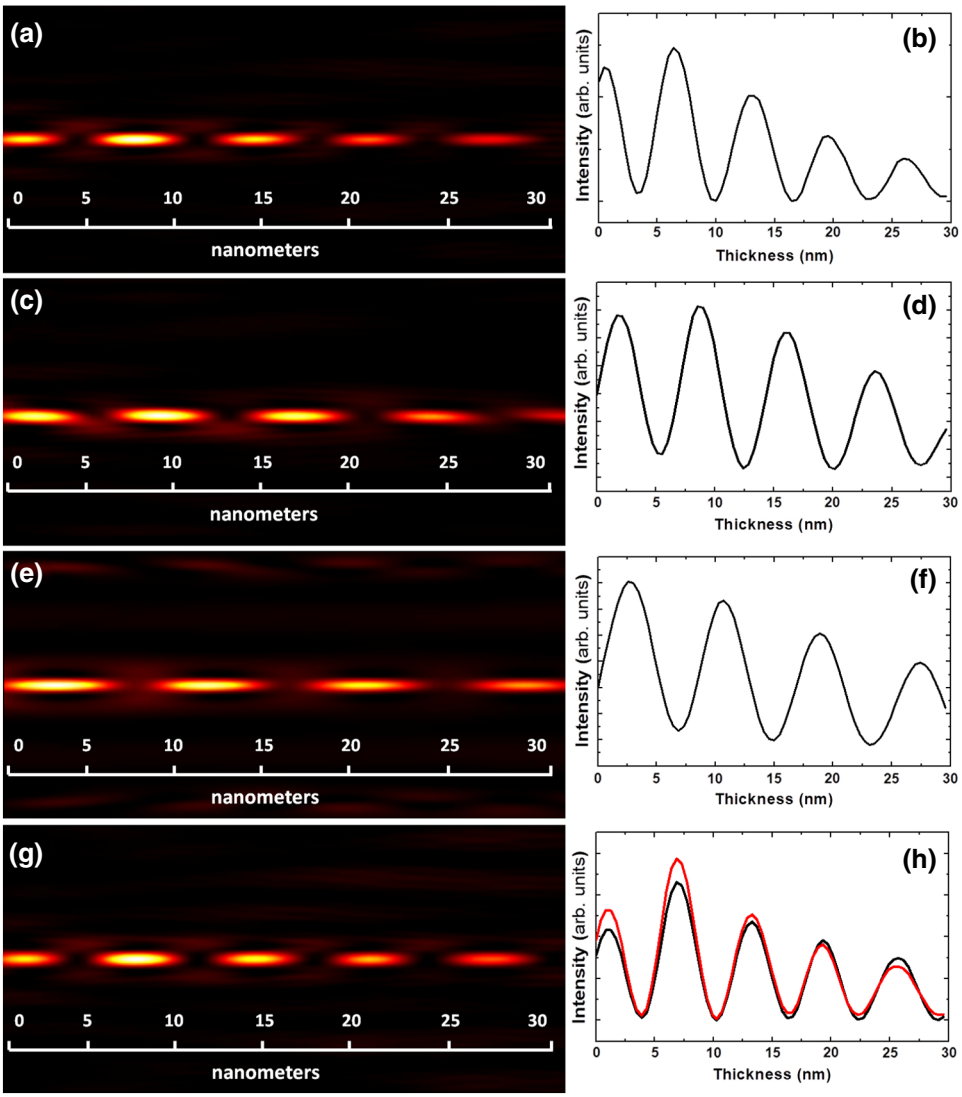

FIG. 4. (a) Multislice simulations of propagation along a Ga column in a [100]-oriented GaN crystal of a Bessel probe formed by (a) a 20–22-mrad ring aperture and (b) its intensity line profile as a function of depth. (c) A 16–18-mrad ring aperture and (d) its intensity line profile as a function of depth. (e) A 14–16-mrad ring aperture and (f) its intensity line profile as a function of depth. (g) A 20–22-mrad ring aperture with 10 nm of defocus and (h) its intensity line profile as a function of depth, with the line profile from (b) shown in red for comparison.

$B_K^{\mathrm{HE}}(\vec{r},z) = J_0(k_{\rho\mathrm{HE}},\vec{r})\exp(iK_z^{\mathrm{HE}}z)$. However, $B_K^{1s}(\vec{r},z)$ can also be approximated, according to Eq. (5), by the Bessel-Gauss function $B_K^{1s}(\vec{r},z) = b^{1s}(\vec{r})\,J_0(k_{\rho 1s}\vec{r})\exp(iK_z^{1s}z)$. The entire beam is, therefore, a superposition of two beating Bessel functions. In a multislice simulation, this point can be highlighted by calculating the probe intensity at oscillation maxima, as demonstrated in Figs. 3(a) and 3(b), which show the formation of two sets of rings with different radii.

The same result is obtained from the Bloch wave calculations. In Figs. 3(c) and 3(d), we report partial wave functions corresponding to the 1*s* state and to the unbound state with transverse energy $-110\ \mathrm{nm}^{-2}$. The Bessel nature of the two states is also clearly visible in this case.

IV. DISCUSSION

A. Engineering the channeling

Having described the properties of Bessel beams, their dependence on chosen parameters can be established. In Fig. 4, multislice simulations of the propagation of Bessel beams are reported for convergence semiangles of a) 20–22 mrad, c) 16–18 mrad, and e) 14–16 mrad. By varying the convergence semiangle, it is possible to vary the frequency of beating along an atomic column. Conversely, if the defocus at the entrance of the sample is changed, no shift of the beating fringes is observed. Figures 4(g) and 4(h) show that the application of 10 nm of defocus to a 20–22-mrad probe is almost negligible. In Fig. 4(h), a profile of a probe without defocus is shown in red. This behavior is explained by the discussion above and by the properties of a Bessel beam in vacuum.

Intelligent use of this behavior can be made in connection with a preceding paper [33], in which we demonstrated that probes with different channeling behaviors can be used to provide three-dimensional information about guest atomic species in a lattice. The contribution of an atom located at depth z to the total image intensity is the product of the probe current at that position $j(z)$ and the atomic scattering cross section. The image contrast can be related to the channeling current $j(z)$ and the distribution of guest species in the column $a(z)$ through the simple relation

$$C = \sum_{i\ \mathrm{atoms}} j(z)a(z). \tag{13}$$

In the specific case of a Bessel beam, the channeling currents $j(z)$ are trigonometric functions, and imaging using different convergence semiangles produces a harmonic decomposition of the unknown function $a(z)$.

B. Optimal channeling probe

Based on the above considerations, we determine an ideal probe that has the same role in a material as a Bessel beam has in vacuum, that is, that propagates in a crystal without diffracting. This problem is equivalent to determining solutions of the wave equation in the material. The answer is well known in microscopy as a two-dimensional Bloch wave solution. Whereas it is complicated to produce a single Bloch wave of arbitrary order that would be delocalized, it is, in principle, possible to produce a beam that resembles a 1*s* state by using beam synthesis techniques. To a large approximation, such a beam can be considered to be a Gaussian beam, as shown in Fig. 5(a). In this case, the beam intensity has a full width at half maximum of 0.35 Å [26], which is close to current instrumental limits [34].

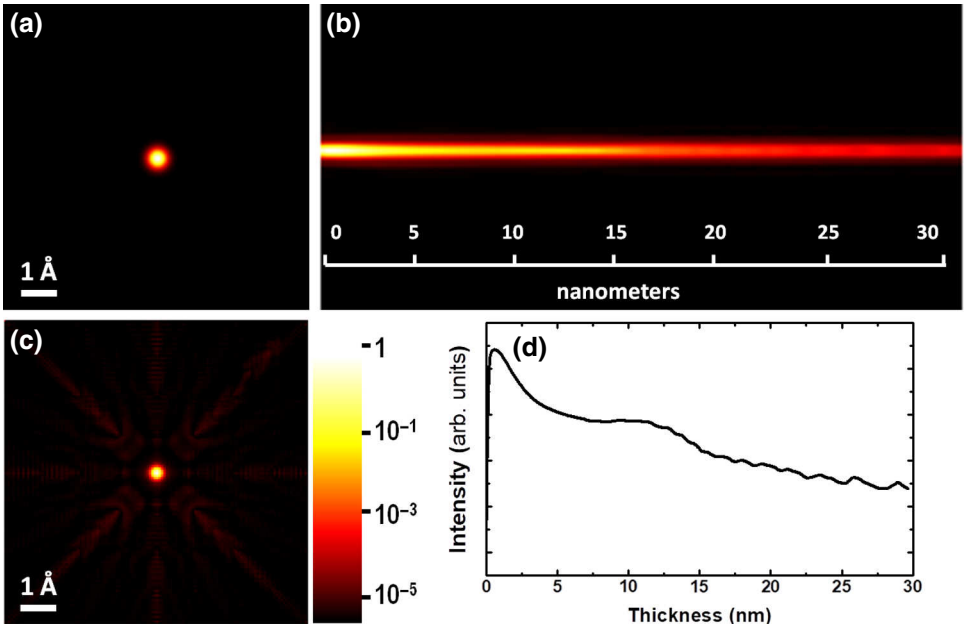

FIG. 5. (a) Simulated image of a Gaussian probe at 300 keV. (b) Its evolution along a Ga column in a [100]-oriented GaN crystal. (c) Simulated image of the Gaussian probe at the exit surface after propagation in the specimen. (d) Intensity line profile plotted as a function of depth.

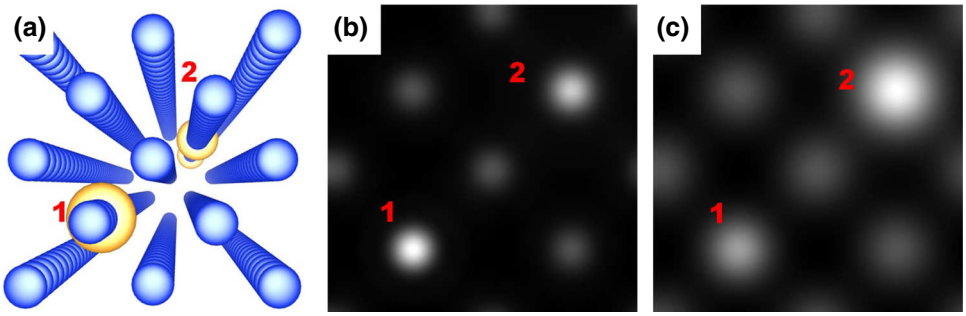

FIG. 6. (a) Atomic model of Si containing one Au atom on top of column "1" and two Au atoms in the center and at the bottom of column "2." (b),(c) Multislice simulation performed using a conventional STEM probe formed by (b) a 20-mrad hard aperture and (c) a Gaussian beam tailored to the Si 1s state (beam waist 0.44 Å).

Figure 5(b) shows a simulation of the propagation of such a probe in a GaN cell, while its depth dependence is shown in Fig. 5(d). The Gaussian probe is still damped, but there is practically no sign of beating between states. Figure 5(c) shows, on a logarithmic scale, that at the end of the propagation, the probe shows very weak signs of crosstalk between adjacent columns.

Such a Gaussian probe appears to be the best suited probe for quantitative, single-column Z contrast STEM experiments. It is well known that column-by-column quantitative analysis is strongly influenced by the propagation of a probe in the sample [35,36]. As a consequence of channeling, the contrast of an atom depends strongly on its depth [37], making quantitative analyses of thin samples unreliable [38]. A Gaussian probe that fits the 1s state of an atomic column can propagate freely, completely avoiding this limitation as shown in Fig. 6, as well as reducing crosstalk to neighboring columns.

As a case study, we consider the imaging of Au impurities in a Si crystal [39,40]. We prepare a 20-nm thick Si (100) supercell containing three Au atoms. The first Au atom is placed on top of a Si column, and is labeled "1" in Fig. 6(a). The other two Au atoms are placed in a column labeled "2," one in the middle of the cell (10 nm below the entrance surface) and the other close to the exit surface. We perform multislice calculations in the "frozen lattice" approximation to simulate an experiment conducted using a conventional STEM probe formed using a 20-mrad hard aperture, as shown in Fig. 6(b), as well as a Gaussian probe tailored to the 1s state of Si (Supplemental Material S4 [26]), as shown in Fig. 6(c). The simulated images are the result of integration over 20 independent thermal "frozen lattice" configurations in order to have a truthful description of the STEM experiment and, in the process, minimize any numerical error.

As a result of the rapid damping of a conventional probe in Fig. 6(b), column (1) containing a single Au atom on top appears brighter than column (2), which contains two Au atoms deeper in the specimen, demonstrating a top-bottom effect. In contrast, for the simulation performed using a Gaussian probe in Fig. 6(c), the high angle annular dark field intensity is proportional to the chemical composition of the specimen, with the column that contains two Au atoms appearing brighter than the column containing only one Au atom. These results, together with the previous considerations, are of great importance for the development of more reliable quantitative electron microscopy and it is potentially a source of great application.

V. CONCLUSIONS

We use Bloch wave and multislice simulations to study the behavior of Bessel and optimal Gaussian electron beams in a material. We consider [100]-oriented GaN with the probe localized on Ga atomic columns. For even states, the probe can be regarded as a superposition of a few relevant states. For example, a 0th-order Bessel probe can be represented as a superposition of two Bessel beams with different z velocities. We compare a Bessel beam with a normal "aperture-limited" probe in order to understand the dynamics of the "pendellösung" oscillation. The observed damping of channeling is due to dispersion of the nonbound states rather than absorption of the 1s states. We also compare our results with those for a Gaussian probe that is optimal for channeling and is of the same size as the 1s Bloch wave in the material. This is the only probe that shows no oscillation in its channeling behavior and is the best-suited probe for quantitative, single-column Z contrast STEM experiments.

ACKNOWLEDGMENTS

This work is supported by Q-SORT, a project funded by the European Union's Horizon 2020 Research and Innovation Programme under Grant No. 766970. The work at the University of Oregon was supported by the U.S. Department of Energy, Office of Science, Basic Energy Sciences, under Grant No. DE-SC0010466. R.D.-B. acknowledges the Deutsche Forschungsgemeinschaft for a Deutsch-Israelische Projektkooperation (DIP) Grant and funding from the European Union's Horizon 2020 research and innovation programme under Grant No. 823717-ESTEEM3. E.K. acknowledges the support of the Canada Research Chair (CRC) program and Ontario's Early Researcher Award (ERA).

[1] O. Scherzer, The theoretical resolution limit of the electron microscope, J. Appl. Phys. **20**, 20 (1949).

[2] V. Intaraprasonk, H. L. Xin, and D. A. Muller, Analytic derivation of optimal imaging conditions for incoherent imaging in aberration-corrected electron microscopes, Ultramicroscopy **108**, 1454 (2008).

[3] K. Watanabe, N. Nakanishi, T. Yamazaki, M. Kawasaki, I. Hashimoto, and M. Shiojiri, Effect of incident probe on HAADF STEM images, Physica Status Solidi B **235**, 179 (2003).

[4] J. Verbeeck, H. Tian, and P. Schattschneider, Production and application of electron vortex beams, Nature **467**, 301 (2010).

[5] B. J. McMorran, A. Agrawal, I. M. Anderson, A. A. Herzing, H. J. Lezec, J. J. McClelland, and J. Unguris, Electron vortex beams with high quanta of orbital angular momentum, Science **331**, 192 (2011).

[6] J. Verbeeck, H. Tian, and A. Béché, A new way of producing electron vortex probes for STEM, Ultramicroscopy **113**, 83 (2012).

[7] V. Grillo, G. C. Gazzadi, E. Karimi, E. Mafakheri, R. W. Boyd, and S. Frabboni, Highly efficient electron vortex beams generated by nanofabricated phase holograms, Appl. Phys. Lett. **104**, 043109 (2014).

[8] V. Grillo, E. Karimi, G. C. Gazzadi, S. Frabboni, M. R. Dennis, and R. W. Boyd, Generation of Nondiffracting Electron Bessel Beams, Phys. Rev. X **4**, 011013 (2014).

[9] V. Grillo, E. Rotunno, B. McMorran, and S. Frabboni, Propagation of Bessel beams along atomic columns in crystal: A Bloch wave and multi-slice analysis, Microsc. Microanal. **21**, 1889 (2015).

[10] T. R. Harvey, J. S. Pierce, A. K. Agrawal, P. Ercius, M. Linck, and B. J. McMorran, Efficient diffractive phase optics for electrons, New J. Phys. **16**, 093039 (2014).

[11] B. J. McMorran, T. R. Harvey, J. Perry-Houts, S. Cabrini, A. Agrawal, and H. Lezec, Sculpting electron beam profile and phase with nanofabricated diffractive optics, EIPBN Proceedings (2012) P04-16.

[12] C. Zheng, T. C. Peterson, H. Kirmse, W. Neumann, M. J. Morgan, and J. Etheridge, Axicon Lens for Electrons Using a Magnetic Vortex: The Efficient Generation of a Bessel Beam, Phys. Rev. Lett. **119**, 174801 (2017).

[13] W. D. Riecke, Z. Naturforsch. Kann man die "atomare Auflösung" im Elektr. mikr. nur mit dem Dunkelfeld erreichen?, **19a**, 1228 (1964).

[14] J. M. Gibson and A. Howie, Investigation of local structure and composition in amorphous solids by high resolution electron microscopy, Chem. Scr. **14**, 109 (1979).

[15] T. Kawasaki, T. Matsutani, T. Ikuta, M. Ichihashi, and T. Tanji, Simulation of a hollow cone-shaped probe in aberration-corrected STEM for high-resolution tomography, Ultramicroscopy **110**, 1332 (2010).

[16] D. T. Nguyen, S. D. Findlay, and J. Etheridge, A menu of electron probes for optimising information from scanning transmission electron microscopy, Ultramicroscopy **184**, 143 (2018).

[17] J. Durnin, J. J. Miceli, and J. H. Eberly, Comparison of Bessel and Gaussian beams, Opt. Lett. **13**, 79 (1988).

[18] B. G. Mendis, Dynamic scattering of electron vortex beams–a Bloch wave analysis, Ultramicroscopy **149**, 74 (2015).

[19] H. L. Xin and H. Zheng, On-column 2p bound state with topological charge ± 1 excited by an atomic-size vortex beam in an aberration-corrected scanning transmission electron microscope, Microsc. Microanal. **18**, 711 (2012).

[20] P. B. Hirsch, A. Howie, R. B. Nicholson, D. W. Pashley, and M. J. Whelan, *Electron Microscopy of Thin Crystals* (Krieger, Huntington, NY, 1977), 2nd ed.

[21] Y. Peng, P. D. Nellist, and S. J. Pennycook, HAADF-STEM imaging with sub-angstrom probes: a full Bloch wave analysis, J. Electron Microsc. **53**, 257 (2004).

[22] A. J. F. Metherell, in *Electron Microscopy in Materials Science II*, edited by U. Valdré and E. Ruedl (CEC, Brussels, 1975).

[23] P. Yu, M. Cardona, *Fundamentals of Semiconductors: Physics and Materials Properties* (Springer, Heidelberg, Germany, 2005), 3rd ed.

[24] P. Geuens and D. VanDyck, The S-state model: a work horse for HRTEM, Ultramicroscopy **93**, 179 (2002).

[25] P. Geuens and D. VanDyck, The S-state model for electron channeling in high-resolution electron microscopy, Adv. Imaging Electron Phys. **136**, 111 (2005).

[26] See Supplemental Material at http://link.aps.org/supplemental/10.1103/PhysRevApplied.11.044072 for a complete analytical derivation of the excited Bloch state energy spectrum and a description of the code used for the calculations. A discussion on the viability of a Gaussian beam fitting the 1s state whit the current state-of-the-art electron microscopes is also reported.

[27] G. R. Anstis, The 1s-state analysis applied to high-angle, annular dark-field image interpretation—When can we use it?, Microsc. Microanal. **10**, 4 (2004).

[28] P. M. Voyles, D. A. Muller, and E. J. Kirkland, Depth-dependent imaging of individual dopant atoms in silicon, Microsc. Microanal. **10**, 291 (2004).

[29] S. J. Pennycook, C. S. Rafferty, and P. D. Nellist, Z-contrast imaging in an aberration-corrected scanning transmission electron microscope, Microsc. Microanal. **6**, 343 (2000).

[30] V. Grillo and E. Rotunno, STEM_CELL: a software tool for electron microscopy: Part 1—simulations, Ultramicroscopy **125**, 97 (2013).

[31] E. J. Kirkland, *Advanced Computing in Electron Microscopy* (Springer, New York, 2010).

[32] V. Grillo, J. Harris, G. C. Gazzadi, R. Balboni, E. Mafakheri, M. R. Dennis, S. Frabboni, R. W. Boyd, and E. Karimi, Generation and application of bessel beams in electron microscopy, Ultramicroscopy **166**, 48 (2016).

[33] E. Rotunno, M. Albrecht, T. Markurt, T. Remmele, and V. Grillo, Three dimensional analysis of the composition in solid alloys by variable probe in scanning transmission electron microscopy, Ultramicroscopy **146**, 62 (2014).

[34] S. Morishita, R. Ishikawa, Y. Kohno, H. Sawada, N. Shibata, and Y. Ikuhura, Attainment of 40.5 pm spatial resolution using 300 kV scanning transmission electron microscope equipped with fifth-order aberration corrector, Microscopy **67**, 46 (2018).

[35] R. R. Vanfleet, M. Robertson, M. McKay, and J. Silcox, Prospects for single atom sensitivity measurements of dopant levels in silicon, AIP Conf. Proc. **449**, 901 (1998).

[36] E. C. Cosgriff and P. D. Nellist, A Bloch wave analysis of optical sectioning in aberration-corrected STEM, Ultramicroscopy **107**, 626 (2007).

[37] P. M. Voyles, J. L. Grazul, and D. A. Muller, Imaging individual atoms inside crystals wit hADF-STEM, Ultramicroscopy **96**, 251 (2003).

[38] E. Carlino and V. Grillo, Atomic-resolution quantitative composition analysis using scanning transmission electron microscopy Z-contrast experiments, Phys. Rev. B **71**, 235303 (2005).

[39] S. H. Oh, K. van Benthem, S. I. Molina, A. Y. Borisevich, W. Luo, P. Werner, N. D. Zakharov, D. Kumar, S. T. Pantelides, and S. J. Pennycook, Point defect configurations of supersaturated Au atoms inside Si nanowires, Nano Lett. **8**, 1016 (2008).

[40] J. E. Allen, E. R. Hemesath, D. Perea, J. L. Lensch-Falk, Z. Y. Li, F. Yin, M. H. Gass, P. Wang, A. L. Bleloch, R. E. Palmer, and L. J. Lauhon, High-resolution detection of Au catalyst atoms in Si nanowires, Nat. Nanotechnol. **3**, 168 (2008).